#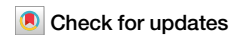 Single-nucleus multiomic analysis of Beckwith-Wiedemann syndrome liver reveals PPARA signaling enrichment and metabolic dysfunction

Check for updates

Snehal Nirgude [1,9], Elisia D. Tichy [1,9], Zhengfeng Liu [2], Sanam L. Kavari[1], Rose D. Pradieu [1], Mariah Byrne [1], Feikun Yang [3], Luis Gil-de-Gómez[4], Brandon Mamou[3], Kathrin M. Bernt [5,6], Wenli Yang[3], Suzanne MacFarland[5,6], Michael Xie[7] & Jennifer M. Kalish [1,6,8] ✉

Beckwith-Wiedemann Syndrome (BWS) is an epigenetic overgrowth syndrome caused by methylation changes in the human 11p15 chromosomal locus. Patients with BWS may exhibit hepatomegaly, as well as an increased risk of hepatoblastoma. To understand the impact of these 11p15 changes in the liver, we performed a multiomic study [single nucleus RNA-sequencing (snRNA-seq) + single nucleus assay for transposable-accessible chromatin-sequencing (snATAC-seq)] of both BWS-liver and nonBWS-liver tumor-adjacent tissue. Our approach uncovers hepatocyte-specific enrichment of processes related to peroxisome proliferator—activated receptor alpha (PPARA). To confirm our findings, we differentiated a BWS induced pluripotent stem cell model into hepatocytes. Our data demonstrate the dysregulation of lipid metabolism in BWS-liver, which coincides with observed upregulation of PPARA during hepatocyte differentiation. BWS hepatocytes also exhibit decreased neutral lipids and increased fatty acid β-oxidation. We also observe increased reactive oxygen species byproducts in BWS hepatocytes, coinciding with increased oxidative DNA damage. This study proposes a putative mechanism for overgrowth and cancer predisposition in BWS liver due to perturbed metabolism.

Beckwith–Wiedemann syndrome (BWS) is a tissue overgrowth disorder resulting from epigenetic alterations on human chromosome 11p15[1,2]. Within the 11p15 region, there are two imprinting centers (IC1 and IC2), whose differential methylation of maternal and paternal DNA origins regulate the expression of the key growth modulators insulin-like growth factor 2 (*IGF2*) and cyclin dependent kinase inhibitor 1 C (*CDKN1C*). Gain of methylation at IC1 (IC1 GOM) leads to biallelic *IGF2* expression, loss of methylation at IC2 (IC2 LOM) leads to decreased *CDKN1C* expression and paternal uniparental isodisomy of chromosome 11p15 (pUPD11) leads to both increased *IGF2* expression and decreased

CDKN1C expression[3]. Both IC2 LOM and pUPD11 cause a wide range of fetal and neonatal overgrowth of the liver, including hepatomegaly, mesenchymal hamartoma and an increased incidence of hepatoblastomas[3,4]. However, the connections between 11p15 chromosome alterations and the downstream molecular cues leading to BWS liver phenotypes have not been well established. Previously, our laboratory conducted a preliminary study of BWS liver, using a bulk RNA sequencing approach, and we found cancer predisposition and oncologic signatures in BWS tumor adjacent liver as well as in hepatoblastoma[3]. Assessing BWS and nonBWS liver tissue in this study provided insight

[1]Division of Human Genetics and Center for Childhood Cancer Research, Children's Hospital of Philadelphia, Philadelphia, PA, USA. [2]Department of Cell and Developmental Biology, Perelman School of Medicine, University of Pennsylvania, Philadelphia, PA, USA. [3]Department of Medicine, Perelman School of Medicine, University of Pennsylvania, Philadelphia, PA, USA. [4]Department of Pediatrics and Center for Childhood Cancer Research, Children's Hospital of Philadelphia, Philadelphia, PA, USA. [5]Division of Oncology, Children's Hospital of Philadelphia, Philadelphia, PA, USA. [6]Department of Pediatrics, Perelman School of Medicine at the University of Pennsylvania, Philadelphia, PA, USA. [7]DBHI, Children's Hospital of Philadelphia, Philadelphia, PA, USA. [8]Department of Genetics, Perelman School of Medicine at the University of Pennsylvania, Philadelphia, PA, USA. [9]These authors contributed equally: Snehal Nirgude, Elisia D. Tichy. ✉e-mail: kalishj@chop.edu

into the functional consequences of 11p15 alterations between the normal and the overgrown liver that contribute to the BWS-specific cancer predisposition signatures, but the previous findings were limited, due to the bulk sequencing approach used. In the current study, a more in-depth analysis of BWS liver was conducted, by examining specific liver cell populations at a single cell level.

The liver is the largest gland and performs both endocrine and exocrine functions. In addition, it executes essential functions, including glycogen storage, detoxification/xenobiotic metabolism, cholesterol synthesis and transport, urea metabolism and secretion of plasma proteins[5,6]. Most importantly, the liver is the key metabolic regulator that systemically governs energy metabolism[7]. About 78% of adult liver volume is composed of hepatocytes, the parenchymal cell type of liver[8]. These hepatocytes coordinate their functions with non-parenchymal cell types, including cholangiocytes, endothelial cells, Kupffer cells, immune cells and hepatic stellate cells[5]. The cellular composition and intracellular signaling of the liver can be comprehensively studied using single cell sequencing approaches. A number of studies have reported detailed single cell maps of adult human liver[9–14], while a study by Wesley et al. described different stages of liver development, including hepatoblast, fetal and adult stages[11]. In the current study, we query the cellular composition and functionality/signaling of hepatoblastoma tumor-adjacent BWS liver compared to hepatoblastoma tumor-adjacent nonBWS liver, as a first step in understanding the mechanisms of BWS overgrowth and liver cancer induction. We have previously reported that in the first year of life, patients with BWS exhibit an elevated alpha fetoprotein (AFP) level, which is typically associated with fetal liver metabolic processes, suggesting that BWS livers are more metabolically active[15]. The combination of hepatomegaly, increased hepatoblastoma risk, and fetal protein expression in BWS livers formed the basis and rationale to build a reference map for BWS pediatric liver at single-nuclei resolution and to query the functionality of overrepresented cell types.

We used the recent technology of multimodal single-nucleus (sn) sequencing to perform parallel RNA-seq+ATAC-seq on isolated single-nuclei from banked flash-frozen tumor-adjacent liver samples. snATAC-seq provides information on chromatin accessible regions of the genome that would otherwise be unavailable by snRNA-seq. snATAC-seq specifically aids in the prediction of cell-type-specific transcription factor activity and identification of distant regulatory regions that influence gene transcription[16]. Using snRNA-seq coupled with snATAC-seq, we performed sequencing on seven pediatric human liver samples, four from BWS and three from nonBWS tumor-adjacent samples. A goal of this study was to generate a detailed map of BWS and nonBWS pediatric liver (normal adjacent to tumor), examining both the cell type composition differences and exploring gene expression changes in BWS liver that may drive its metabolic activity. snRNA-seq identified similar cellular types between both cohorts; however, cellular pathways related to fatty acid and lipid metabolism, as well as PPARA signaling, were all enriched in BWS liver hepatocytes, when compared to those of nonBWS liver hepatocytes. snATAC-seq uncovered differential chromatin accessibility for these signaling pathways, with increased accessibility in the BWS livers. Since BWS modeling in the mouse has limitations[17], we differentiated BWS-induced pluripotent stem cells (iPSC) into hepatocytes to validate the findings from our sn-multiome dataset. When BWS-iPSC and control lines were subjected to hepatocyte differentiation, we found enrichment of fatty acid and lipid metabolism pathways in BWS lines, similar to the BWS patient liver hepatocytes. Using RNA-seq and real-time qPCR approaches, we demonstrated enrichment of PPARA in BWS lines relative to control lines, as differentiation proceeded. We additionally scored iPSC-derived hepatocytes for changes to fatty acid metabolic properties and found a decreased presence of neutral lipid droplets, concomitant with increased fatty acid β-oxidation in the BWS lines, indicating alterations in the metabolic activity of BWS hepatocytes. Finally, we found an increased reactive oxygen species (ROS) response, concomitant with an increase in oxidative DNA damage in the BWS

hepatocytes. We propose here a mechanism that defines the molecular setup of neoplastic transition in BWS-livers driven by metabolic perturbations.

Results
Clinical cohort
The patient sample information can be found in Supplementary Table 1 and includes samples from 4 BWS patients (2 IC2 LOM, 2 pUPD11) and 3 nonBWS patients. This study utilized cohorts with as closely matched ages and sexes as was feasible and available within the institutional biobank. Histologic review of tumor-adjacent tissue revealed similar liver gross morphologies between both BWS and nonBWS groups (Supplementary Fig. 1a, 1b); however, we did observe differences in the hepatocyte populations. Specifically, when we calculated hepatocyte sizes in both cohorts, we found that BWS liver had smaller and more numerous hepatocytes, relative to nonBWS livers (Supplementary Fig. 1c), which may contribute to reported BWS hepatomegaly. We confirmed the methylation status of the two imprinted regions on chromosome 11p15 (H19-IC1 and KvDMR-IC2) in both nonBWS and BWS liver samples by performing pyrosequencing for KvDMR and H19 (Supplementary Fig. 2a-2d). The nonBWS livers exhibited normal methylation at both IC1 and IC2, while the BWS samples were either IC2 LOM ($n = 2$) or pUPD11 ($n = 2$), consistent with clinical testing results in blood (Supplementary Table 1).

The landscape of cells in the BWS and nonBWS livers
snRNA-seq and snATAC-seq were performed on the four BWS livers and three nonBWS livers (Fig. 1a). We used Seurat (version 4)[18–21] and Harmony[22] packages to determine the cellular composition of the snRNA-seq samples and annotate cells based on their transcriptional profiles. After quality control filtering and removal of putative doublets, we obtained the snRNA-seq profile for 74,315 nuclei. Using an unsupervised clustering approach, we identified 7 cell populations represented by 18 cell clusters that identified both parenchymal and non-parenchymal liver cells in both BWS and nonBWS livers (Fig. 1b, c). Their composition included hepatocytes, cholangiocytes, hepatic stellate cells, Kupffer cells, endothelial cells, and immune cells. We performed annotation using SingleR, ScType, as well as manual annotation methods. For manual annotation, we obtained markers using the FindClusters function from Seurat (Supplementary Data File 1 – **Top 50 cell markers in each cluster**) and we observed cell-type-specific expression of a number of genes (Fig. 1d, 1e). We identified hepatocytes using known markers defined in previous liver studies, including: *ALB, ACSL4, FGG, FGA, CYP3A4, PCK1, CPS1, CP, ASGR1, APOC1* and *CYP2E1*[9,13,14]. Using these genes, we identified seven clusters (Cluster 0, 1, 7, 12, 14, 15, and 17) representing hepatocytes. Clusters 0, 1, and 7 were the predominant hepatocyte clusters, as hepatocyte clusters 12, 14, 15, and 17 had fewer than 500 nuclei. Using *KRT7, KRT19* and *CDH1* markers, we identified two clusters (Cluster 3 and 10) representing cholangiocytes[13,14]. Two clusters (Cluster 5 and 8) of hepatic stellate cells were identified by *IGFBP7, PDGFRA, COL3A1* and *DCN* markers. The *CD163* marker identified the clusters for Kupffer cells (Clusters 4, 13) and the PTPRC marker identified the clusters for the immune cells (Clusters 6 and 11)[13,14]. Three clusters (Clusters 2, 9, and 16) representing distinct endothelial cells were identified using markers *FLT1, RELN, CLEC4M, CTSL* and *PECAM1*[13,14]. Major cell types and their relative abundance were identified in both liver groups (BWS and nonBWS) (Fig. 1f). Specifically, in BWS livers, hepatocytes represented ~62% of total analyzed nuclei, whereas cholangiocytes, hepatic stellate cells, Kupffer cells, immune cells and endothelial cells represented 5%, 10%, 6%, 4%, and 10% respectively. In nonBWS livers, hepatocytes represented ~55% of total analyzed nuclei, whereas cholangiocytes, hepatic stellate cells, Kupffer cells, immune cells and endothelial cells represented 11%, 6%, 8%, 4%, and 14%, respectively. These findings demonstrate that BWS livers contain more hepatocytes, in agreement with our histological examination and which may contribute to the hepatomegaly often observed in BWS patients[3].
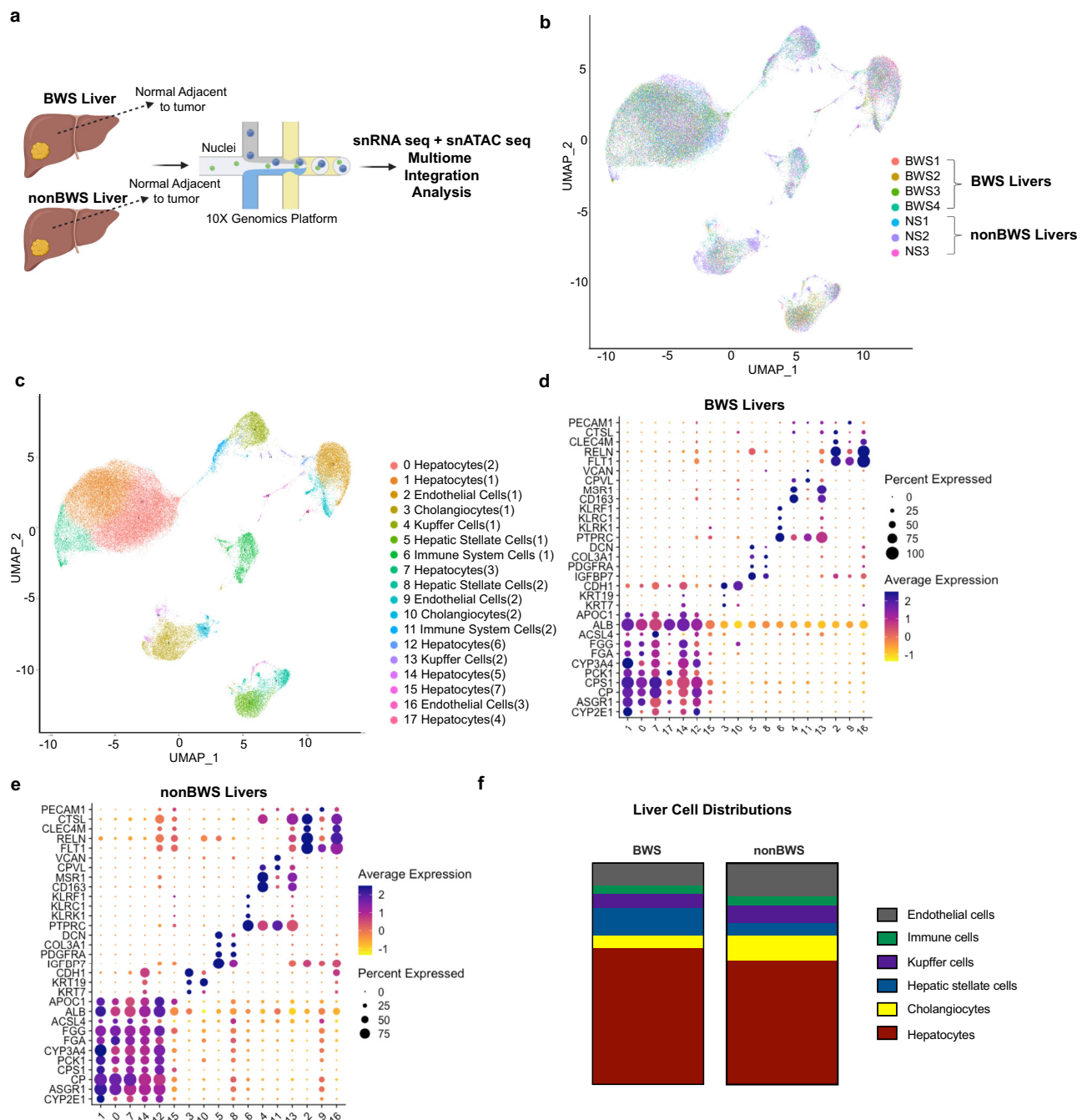
Fig. 1 | snRNA-seq profiles of BWS and nonBWS livers. a Schematic of our multiomics study. Single nuclei were isolated from 4 BWS and 3 nonBWS tumor-adjacent liver samples and prepared for snRNA-seq using the 10X Genomics technology. Created with BioRender.com **b** UMAP visualization 74,315 liver nuclei isolated from 7 liver samples. **c** The uniform manifold approximation and projection (UMAP) of BWS (*n* = 4) and nonBWS (*n* = 3) livers using snRNA-seq demonstrates that both liver groups contain the same cell types clustered into 18 cell subpopulations. This transcriptome atlas identified major liver cell types including hepatocytes, cholangiocytes, hepatic stellate cells, Kupffer cells, endothelial cells and immune system cells in both BWS and nonBWS livers. Dot plots of snRNA-seq dataset showing gene expression patterns of cluster-enriched markers for BWS liver (**d**) and nonBWS livers. **e** The diameter of the dot corresponds to the proportion of cells expressing the indicated gene and the density of the plot corresponds to average expression relative to all cell types. **f** Stacked column graphs displaying the average cell type distribution percentages between BWS (left) and nonBWS (right) livers. The percentages from each individual color add up to the total number of cells in that sample type.

Characterization of BWS liver hepatocytes

Since hepatocytes are the major cell population of the liver and our data showed this population is more represented in BWS, we focused on the function and dysregulation of this population. Hepatocytes perform various functions of the liver, including: fatty acid metabolism, xenobiotic metabolism, retinoid metabolism, and iron homeostasis. To query whether BWS hepatocytes were altered in function, compared to nonBWS hepatocytes, we examined the gene expression profiles of these processes, using the documented gene sets of functional pathways for the liver reported by Payen et al. [12]. (Supplementary Table 2). We compared the expression profile of these gene sets in our three major clusters of hepatocytes (Cluster 0,1,7) which contained >500 nuclei comprising each cluster. Other hepatocyte clusters were excluded from the analysis due to the low representation of the population. All the genes in pathways
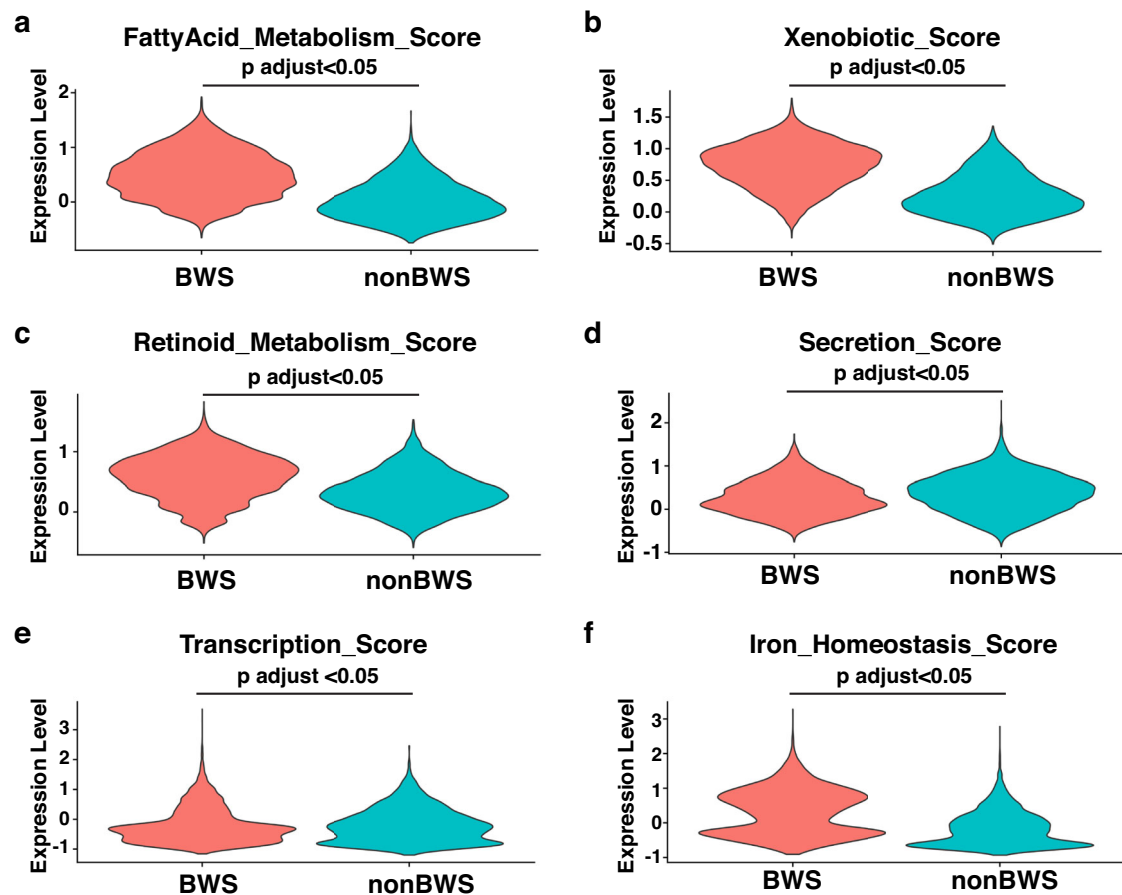
Fig. 2 | Hepatocyte functionality of BWS and nonBWS liver. Violin plots of hepatocyte representing clusters 0, 1, and 7 examining filtered gene lists for fatty acid metabolism (**a**), xenobiotic metabolism (**b**), retinoid metabolism (**c**), secretory functions (**d**), transcription (**e**), and iron homeostasis (**f**). These gene lists were curated from[12]. $n = 4$ BWS and $n = 3$ nonBWS livers.

reported by Payen et al. [12],—fatty acid metabolism, xenobiotic metabolism, retinoid metabolism, transcription factor, secretion of plasma proteins and iron homeostasis, were expressed in both BWS and nonBWS liver hepatocytes, confirming that our hepatocyte clusters function as expected (Fig. 2). However, the BWS hepatocytes exhibited enhanced expression of several processes, including fatty acid metabolism, xenobiotic metabolism, retinoid metabolism, and the iron homeostasis pathway, when compared to nonBWS livers (Fig. 2). These interesting observations led us to further characterize BWS hepatocyte functionality.

Integration of snRNA and snATAC datasets predicted the transcription factor-gene regulation network

To understand the transcriptomic regulation of genes, we performed snATAC-seq and captured the chromatin accessibility profile of individual liver cells. Since less is known about the cell type-specific chromatin accessibility profiles of liver cells, we used our annotated snRNA-seq dataset to predict the snATAC-seq cell types. Using shared barcodes from joint multiomics profiling and ArchR[23], we performed the snATAC-seq cell annotation, which represented the 18 cell subpopulations in the snATAC-seq dataset for both liver cohorts (Fig. 3a, b). We found 25,472 snATAC-seq marker peaks enriched in cell-type specific manner in BWS liver (Fig. 3c) and 19,772 snATAC-seq marker peaks enriched in nonBWS liver (Fig. 3d). These peaks were enriched in promoter, distal, intronic and exonic regions for both livers. To understand the underlying transcription factor—gene regulation network that makes BWS hepatocytes distinct from nonBWS ones, we integrated the snRNA-seq data with snATAC-data by utilizing single-cell regulatory network inference and clustering (SCENIC +)[24]. We

performed this analysis by subsetting the three major hepatocyte clusters that have at least 500 nuclei (Cluster 0, 1, and 7), present in both cohorts. By comparing the hepatocytes from both BWS and nonBWS liver groups, we identified 27 activating enhancer-regulons networks (eRegulons). (Fig. 3e, Supplementary Data File 2—**List of all eRegulons regulated in hepatocytes of BWS liver**). The most significant upregulated activating eRegulons in BWS were Peroxisome Proliferator-Activated Receptor α (PPARA), its binding partner, Retinoid X Receptor Alpha (RXRA), and Transcription Factor 7 Like 1 (TCF7L1). We then studied the expression pattern of these eRegulons using our snRNA-seq data. The violin plots show that PPARA, RXRA and TCF7L1 are more enriched in BWS hepatocytes when compared to the nonBWS hepatocytes (Supplementary Fig. 3a–3c). We also verified the expression of three eRegulons (TCF12, SMAD5 and SOX6) that were enriched in nonBWS hepatocytes using the snRNA-seq data (Supplementary Fig. 3d–3f). Further, we generated an interactome map of PPARA and RXRA eRegulons (Supplementary Fig. 4), since PPARA and RXRA are interacting partners in various liver functional pathways[25]. These pathways include the production and breakdown of lipids and amino acids[26], and dysfunctional PPARA signaling is implicated in hepatocyte proliferation[27] and hepatomegaly[28], while TCF7L1 is a WNT signaling regulator and is implicated in cell stemness[29,30]. Thus, using SCENIC + , we constructed a regulatory network from our single-nuclei multiomic dataset which showed enrichment of PPARA and RXRA.

Gene ontology (GO) analysis reveals altered metabolic pathways in BWS livers

To understand the biological processes regulated by eRegulons enriched in the BWS livers, we performed Gene ontology (GO) term analysis using the
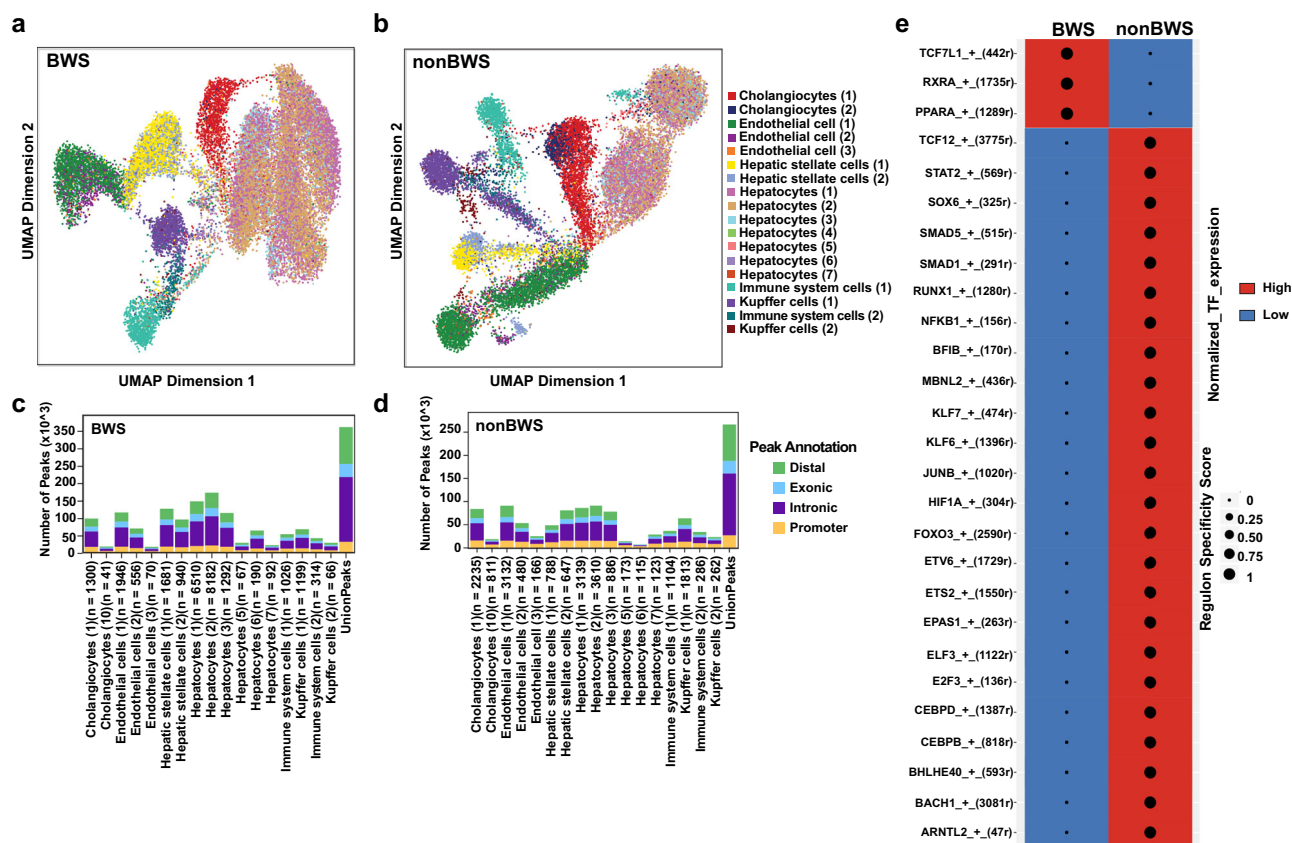
Fig. 3 | Chromatin accessibility profiles from joint snRNA-seq and snATAC-seq of the BWS and nonBWS livers. The uniform manifold approximation and projection (UMAP) of BWS (*n* = 4) and nonBWS (*n* = 3) livers using snATAC-seq with cell annotation predicted from snRNA-seq dataset for BWS liver (**a**) and nonBWS liver (**b**). All 17 cell subpopulations representing major cell types in the liver are represented. Bar plot of annotated differentially accessible region (DAR) locations for each cell type in BWS liver (**c**) and nonBWS liver (**d**). **e** Heatmap showing transcription factor expression and group specificity of the eRegulon are displayed using SCENIC + . The activating eRegulons with calculated region-to-gene correlation coefficients (rho) bigger than 0.6 are included in the graph. Red: high normalized transcription factor expression; Blue: low normalized transcription factor expression.

snRNA-seq data on the major hepatocyte clusters (Cluster 0,1,7) captured in the BWS livers in comparison to nonBWS livers. Figure 4a–c depicts the GO terms enriched in the Cluster 0, 1 and 7 from the snRNAseq dataset representing Hepatocytes (2), Hepatocytes (1) and Hepatocytes (3) cell types in the ATACseq dataset. We found many GOBP terms regulated by the PPARA and RXRA eRegulon that were enriched in BWS hepatocytes, such as amino acid metabolic processes, fatty acid/lipid metabolic process, steroid metabolism, and xenobiotic metabolism. In addition, the GOBP_Regulation_of_WNT_signaling_pathway term related to the TCF7L1 eRegulon was also enriched in the BWS Hepatocytes cluster 1. PPARA is a major regulator of fatty acid metabolism and lipid metabolism in liver[31,32], and hepatocytes from BWS livers were enriched in many PPARA-associated downstream processes. We also found PPARA as an enriched motif in our snATAC-seq dataset (Supplementary Data File 3—**Enriched motifs in BWS liver**). We next studied an interaction network of all enriched motifs (with chromatin accessibility) in BWS liver using STRING database[33] and extracted all the interactions related to fatty acid metabolism. We found that PPARA was one of the most interacting genes of this interactome (Supplementary Fig. 5). We also characterized the expression of PPARA-specific gene targets and processes, previously categorized in the mouse liver by Szalowska et al. [34]. This analysis, which the authors coined as "PPARα tailored analysis" set out to identify and categorize gene sets that were enriched following PPARA agonist treatment but not altered in PPARA knockout mice treated with this agonist. We found several PPARA-dependent processes using the Szalowska gene lists that were markedly upregulated in BWS hepatocytes, including retinoid metabolism, peroxisomal β-oxidation, mitochondrial β-oxidation, and intracellular oxysterols

receptors (Supplementary Table 3, Fig. 4d–g). We extended our findings to include other energy related processes, given that β-oxidation of fats is a catabolic process used to generate energy[7,35,36]. We found many of the PPARA processes described by Szalowska et al. were not expressed in our datasets, likely due to the differences between single cell and single nucleus RNA sequencing. However, several functions were expressed at very low levels in both BWS and nonBWS hepatocytes, including carnitine transporters, glycogen metabolism, lipogenesis, lipid mobilization, peroxisomal membrane and biogenesis, and synthesis of lipid precursors (Supplementary Fig. 6). Other PPARA processes were expressed at higher levels in BWS and nonBWS hepatocytes, including the lipoprotein, cholesterol biosynthesis, and inhibition of TG lipases categories (Supplementary Fig. 6). These findings suggest that, in addition to retinoid storage alterations, BWS hepatocytes are more enriched in pathways of fatty acid catabolism for energy derivation by β-oxidation and less enriched in signals that inhibit the degradation of fats (TG Lipases). In aggregate, our data demonstrate that hepatocyte-specific PPARA signaling changes are a major contributor to the altered liver environment in BWS.

BWS iPSC-derived hepatocyte model depicts the metabolic nature BWS livers
We next performed in vitro studies to validate our findings of PPARA dysregulation in BWS hepatocytes. We generated two BWS-iPSC lines from a parental control line using a CRISPR-Cas9 approach. We deleted a ~ 1.7 kb fragment of the maternal strand IC2 region from the parental line (Supplementary Fig. 7a). This region is included in several previously reported BWS patient-specific deletions[37–41]. Both edited iPSC lines

Fig. 4 | PPARA functionality testing in BWS patient hepatocytes. a–c Top GO terms with highest fold change, (adjusted p value < 0.05) and enriched in the three hepatocytes clusters (Cluster 0, 1, 7) of BWS livers ($n = 4$) when compared to nonBWS ($n = 3$) livers were plotted. Processes in orange are known PPARA downstream functions. **d–g** Violin plots of gene expression categories PPARA tailored analysis, curated from[34]. Wilcoxon p values were all less than 0.05.
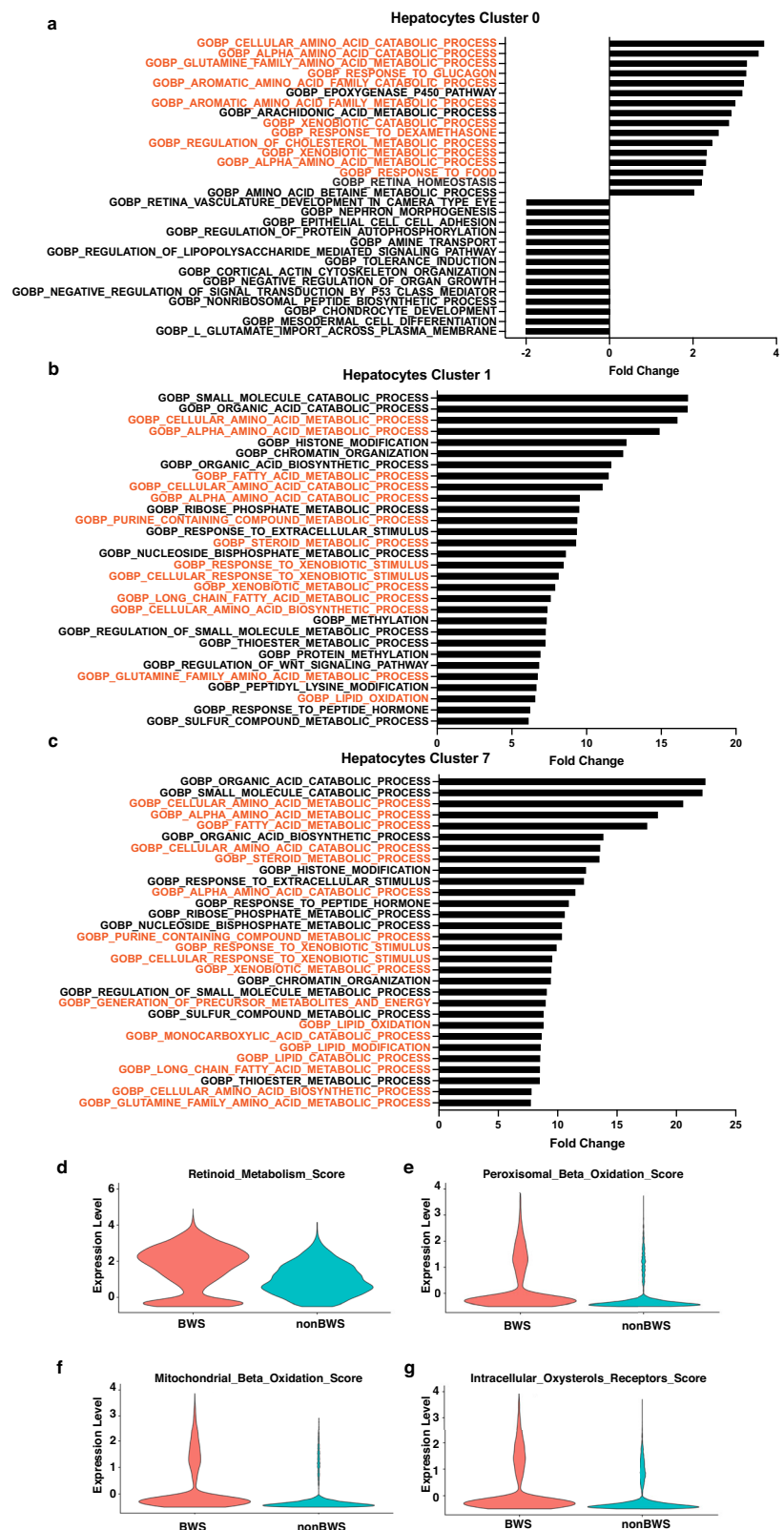
displayed a normal karyotype (Supplementary Fig. 7b, 7c). We differentiated these lines down a hepatic lineage and queried the methylation status of chromosome 11p15 by pyrosequencing on Day 0 (iPSC stage), Day 10 (hepatic progenitor stage), as well as on Days 15, 18, and 20 (hepatocyte stages) (Supplementary Fig. 7d, 7e), to ensure hepatocyte differentiation did not affect the BWS critical region. We found that our engineered BWS iPSC lines had the expected 11p15 methylation profile, which was retained during hepatocyte differentiation. We further characterized the edited lines by examining the expression of BWS-relevant IC2 genes. We found reductions in *CDKN1C* expression, decreases in *KCNQ1* expression, and increases in *KCNQ1OT1* expression (Supplementary Fig. 7f), consistent with a BWS IC2 phenotype. We also confirmed that there were no defects in the early
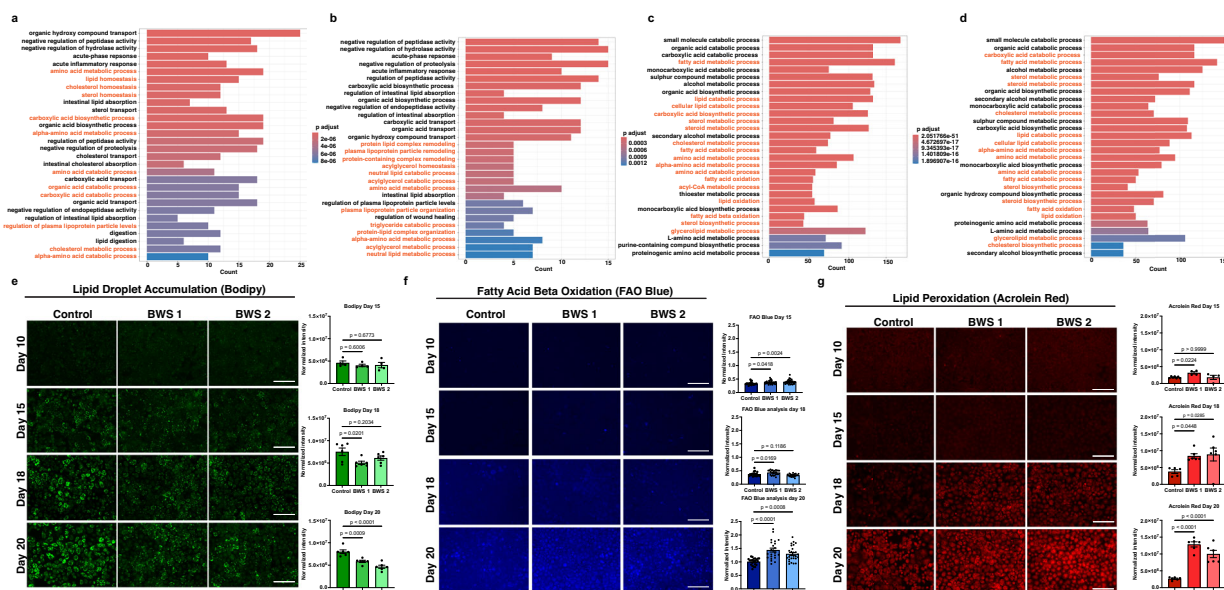
Fig. 5 | Hepatocyte-specific BWS effects on PPARA signaling and fatty acids in vitro. GO term enrichment plot for Day 15 of hepatocyte differentiation in BWS 2 (**a**) and BWS 1 (**b**) line when compared to Day 15 of hepatocyte differentiation in the control line. GO term enrichment plot for Day 20 of hepatocyte differentiation in BWS 2 (**c**) and BWS 1 (**d**) line when compared to Day 20 of hepatocyte differentiation in the parental line. Live cell imaging of control, BWS 1, and BWS 2 cells undergoing differentiation and stained with Bodipy (lipid droplets) (**e**), FAO Blue (fatty acid β-oxidation) (**f**), and Acrolein Red (lipid peroxidation) (**g**). Quantification for days 15, 18, and 20 of differentiation are shown beside the image and represent the mean ± SEM of the background-corrected raw intensity value divided by cell number. *p* values were generated by one way ANOVA. At least 2 biological replicates are displayed per time point.

differentiation process into endoderm by performing quantitative RT-PCR at Day 5 of differentiation for relevant markers (*CXCR4, FOXA2, SOX17*)[42] (Supplementary Fig. 8). These markers showed no significant differences, relative to the control parental line, demonstrating that BWS iPSC lines had no alterations in the early stages of differentiation. We further examined the efficiency of hepatocyte differentiation by RNAseq at day 0, day 15, and day 20 of differentiation. First, we examined PCA plots at day 15 and day 20 (Supplementary Fig. 9a, 9b), which showed that the BWS lines were similar to each other at both time points. We then queried the changes in expression profile of several functional hepatocyte genes on days 0, 15, and 20 of differentiation. We observed the expected increase in expression of the markers (*ALB, ASGR1, HGD, HNF1A, HNF4A*) in both control and BWS lines, demonstrating that no defects in hepatocyte differentiation programming exist in BWS lines (Supplementary Fig. 9c-9e). Then we performed GO term enrichment analysis on Day 15 and Day 20 hepatocyte-differentiated lines. Compared to the control line on Day 15 and Day 20, we found upregulation of PPARA-associated processes, including fatty acid and lipid metabolic processes (Fig. 5a–d) in line with GO term enrichment analysis and PPARA tailored analysis of BWS hepatocyte snRNA-seq analysis (Fig. 4). These data confirm that our modified iPSC lines behave similarly to BWS patient hepatocytes in regard to changes in PPARA-involved metabolic processes. To determine whether other aspects of our iPSC model recapitulate our observations in BWS livers, we monitored the changes in cell size during hepatocyte differentiation between control and BWS lines (Supplementary Fig. 10). Size analysis using phalloidin staining to mark cell boundaries displayed smaller hepatocytes in BWS-altered cells relative to control, in line with what was observed in BWS liver. Additionally, phase contrast imaging demonstrated BWS hepatocytes exhibited reductions in lipid droplet accumulation (Supplementary Fig. 10). Since PPARA was enriched in hepatocytes in our multiomic study and it is a major regulator of lipid metabolism in the liver, we studied expression of PPARA over a differentiation time course in our iPSC-differentiated hepatocytes. We first performed qRT-PCR for PPARA on Day 10, Day 15, Day 18 and Day 20 of hepatocyte differentiation. We found that PPARA expression increased over the course of differentiation in BWS cells compared to control and was the highest at day 20 (Supplementary Fig. 11a–11d). We

then confirmed these data in our iPSC RNAseq dataset at day 20 (Supplementary Fig. 11e), again finding increased expression of PPARA. These findings are consistent with our multiomic analyses displaying the upregulation of PPARA in BWS patient hepatocytes and further validate our iPSC model as properly recapitulating BWS phenotypes.

BWS iPSC-derived hepatocytes exhibit altered lipid metabolism
Since PPARA is involved in cellular processes that include lipid metabolism[31,32], we next examined the effects of BWS-specific PPARA upregulation on several lipid processes. We first confirmed our morphological study that suggested differences in lipid droplet accumulation in iPSC-derived BWS hepatocytes using a functional readout. Bodipy 493, a cell permeable nonpolar dye, accumulates in neutral lipid droplets and fluoresces when bound to neutral lipids[43,44]. We found that the fluorescence intensity following Bodipy staining increased over differentiation time in both control and BWS lines (Fig. 5e), indicating increases in lipid droplet formation. However, this increase over time was much more pronounced in control lines when compared to BWS lines. This finding can be explained by an increase in fatty acid breakdown through fatty acid β-oxidation and/or less production of fats. Since PPARA target genes include enzymes in the β-oxidation pathway, and we observed enriched fatty acid β-oxidation gene expression in our BWS hepatocyte snRNAseq PPARA tailored analysis (Fig. 4e, f), we assessed lipid breakdown by utilizing a commercially available fluorescent indicator FAO blue[45,46]. This cell permeable dye is colorless until it is processed by the fatty acid β-oxidation cycle, where it becomes a quantifiable fluorescent marker. Staining cells with this dye revealed that β-oxidation activity increases in both control and BWS hepatocytes over our differentiation time course (Fig. 5f). By Day 20, BWS hepatocytes exhibited significantly more β-oxidation when compared to control hepatocytes. These findings agree with our previous data demonstrating PPARA gene expression is highest in BWS lines at day 20 (Supplementary Fig. 11). To further confirm these results, we performed unbiased assessments of our day 15 and day 20 iPSC to hepatocyte RNAseq dataset, using a filtered gene list of β-oxidation processes. We observed positive enrichment of several β-oxidation genes in both BWS lines at day 15, relative to control (Supplementary Fig. 12a, 12b). However, by day 20 of differentiation, we observed

that most of the gene set was significantly and positively enriched in both BWS lines, relative to control (Supplementary Fig. 12c, 12d). Additionally, we found PPARA to be significantly positively enriched in both BWS lines, and it was the highest positively-enriched gene of this process in BWS 1. In aggregate, these findings depict an altered metabolic environment in BWS hepatocytes, with increased breakdown of lipids for downstream metabolic processes.

BWS iPSC-derived hepatocytes display increased ROS signatures

A consequence of β-oxidation is the generation of endogenous reactive oxygen species (ROS)[47,48], which, among other effects, can lead to lipid peroxidation. To assess whether iPSC-derived BWS hepatocytes exhibit more ROS, we performed acrolein red staining, which uses a fluorescent indicator as a functional readout to measure lipid peroxidation caused by oxidative stress[49,50]. As observed in Fig. 5g, BWS hepatocytes showed enrichment in acrolein red staining when compared to control hepatocytes, particularly at later time points examined. These findings are suggestive of a role for increased PPARA in the BWS-hepatocytes contributing to increased fatty acid oxidation, which subsequently coincides with increase in lipid peroxidation, a marker of oxidative stress. To confirm our findings, we again conducted an agnostic study in our iPSC to hepatocyte RNAseq dataset, using a reactive oxygen species filtered gene list. We found similarly affected genes in both lines, with only a small number positively enriched at day 15 (Supplementary Fig. 13a, 13b). By day 20 of the differentiation process, there was a clear positive increase in the expression of genes involved in ROS signaling in BWS lines (Supplementary Fig. 13c, 13d). Inappropriate ROS formation has many deleterious cellular consequences, including the formation of DNA damage[51]. Since BWS livers are more prone to tumorigenesis, we next examined the level of oxidative stress and DNA damage in our iPSC to hepatocyte model. We again utilized our RNAseq dataset and examined oxidative stress signaling at day 15 and day 20 of differentiation using an oxidative stress filtered gene list. We found downregulation of p53 and its downstream target GADD45A, and upregulation of the E3 ubiquitin ligase RCHY1, which targets p53 for degradation[52], in BWS hepatocytes relative to control at day 15 (Supplementary Fig. 14a, 14b). The tumor suppressive role of p53 is well-established, and its downregulation could be a contributing factor by which BWS liver can transition from normal to cancer. More surprisingly, we observed positive gene enrichment in DNA replication fork collapse-responsive genes (RAD51D, SAMHD1, and ZRANB3)[53,54], oxidative DNA damage repair genes (OGG1, MGMT)[55], and several antioxidant genes (CAT, GPX7, PRDX3, and SOD2)[56] between day 15 and day 20 of differentiation in BWS hepatocytes (Supplementary Fig. 14c, 14d). We next confirmed some of these findings by examination of control and BWS hepatocytes at day 20 of differentiation, and staining cells for the presence of the ROS-damaged DNA base, 8-oxoguanine. We found BWS hepatocytes exhibited more oxidative DNA damage, relative to control, and this finding was also correlated with increased expression of OGG1, a key enzyme in the removal of 8-oxoguanine DNA damage, in BWS lines (Supplementary Fig. 14c–14f). In aggregate, these findings demonstrate BWS iPSC-derived hepatocytes are more metabolically active and exhibit more oxidative stress and DNA damage, which in patients, may contribute to the development of hepatoblastoma.

Discussion

The purpose of this study was to characterize BWS liver tissue and discover BWS-specific transcriptional and functional alterations compared to nonBWS livers. We examined the transcriptome and chromatin accessibility profile of BWS and nonBWS pediatric liver in an unbiased manner using a single nuclei multiomic sequencing approach. This approach revealed enrichment of the PPARA, a liver metabolic regulator, in BWS hepatocytes[31,57]. To confirm our findings, we generated a BWS-iPSC model and differentiated them into hepatocytes. Our in vitro data demonstrates the

dysregulation of lipid metabolism in BWS-hepatocytes, which coincided with observed upregulation of PPARA during hepatocyte differentiation. BWS liver hepatocytes exhibited decreased neutral lipids, increased fatty acid β-oxidation, and ROS-related processes, relative to controls. We propose that the altered liver metabolism in BWS liver is a major contributor to hepatomegaly and cancer predisposition to hepatoblastoma, based on the presence of ROS-related DNA damage.

We captured a comprehensive map of 74,315 nuclei from a total of seven hepatoblastoma tumor-adjacent liver samples, broken down into 4 BWS and 3 nonBWS patients. Using the markers for liver cells described previously in adult liver studies[9,10,12], we identified both parenchymal and non-parenchymal liver cells in both the cohorts. Payen et al. described genes for specific liver functions like xenobiotic metabolism, fatty acid metabolism, retinoid metabolism, secretion of plasma proteins, transcription factor activity and iron ion homeostasis for hepatocytes[12]. We observed enrichment of these liver functional genes in BWS hepatocytes, relative to nonBWS hepatocytes. These data suggest that BWS livers have a distinct, dysregulated metabolic profile compared to nonBWS liver.

To further understand the gene regulation differences in our liver hepatocyte cohorts, we used an integrated approach by combining our snRNA-seq and snATAC-seq data. SCENIC+ analysis utilized this integrated dataset and was used to understand the transcription factor/gene regulation network that defines BWS patient hepatocytes, where we found activation of PPARA and RXRA. PPARA is a ligand-activated nuclear receptor highly expressed in the liver parenchymal cell population i.e. the hepatocytes[25,32]. PPARA is known to form heterodimers with RXRA and functions as a master regulator of hepatic lipid metabolism, including fatty acid synthesis, fatty acid β-oxidation, fatty acid uptake and binding, lipid droplet metabolism, lipoprotein metabolism, glycerol metabolism and cholesterol/bile metabolism, amino acid metabolism, inflammation, and energy metabolism[25,58]. Our GO term enrichment studies in the hepatocytes comparing BWS to nonBWS liver demonstrated an enrichment of fatty acid and lipid metabolic pathways in BWS hepatocytes, indicative of PPARA involvement in the dysregulation of these processes in BWS liver. To validate our findings, we investigated PPARA downstream targets using a published PPARA tailored analysis[34]. We found several PPARA-specific processes upregulated in BWS hepatocytes from patient livers, including an enrichment of fatty acid β-oxidation pathways and oxysterol binding proteins. Oxysterols are oxidation products of cholesterol and play important roles in cholesterol homeostasis[59]. Oxysterols can also serve as secondary signaling messengers in physiological and pathological contexts[60]. Pathological oxysterols formation are often results of ROS and secondary products of lipid peroxidation[61], and their production can be balanced by the activity of antioxidants, such as catalase, superoxide dismutase, and glutathione peroxidase[60].

Modeling BWS hepatocytes using our iPSC lines recapitulated several of our observations in BWS patient liver samples, including exhibiting significant upregulation of PPARA at later stages of the hepatic differentiation process. To understand the impact of PPARA upregulation in downstream metabolic processes in our system, we assayed the lipid accumulation, fatty acid β-oxidation and lipid peroxidation in the BWS-iPSC differentiated hepatocytes and found changes in all examined lipid metrics in BWS hepatocytes. A hallmark of hepatocyte functionality is the accumulation of neutral lipid droplets[57,62]. In our BWS iPSC hepatic differentiation system, we observed neutral lipid accumulation in hepatocytes, particularly at later time points of differentiation. However, as compared to the control line, which had progressive lipid droplet formation during differentiation, the BWS-hepatocytes exhibited reduced lipid droplet accumulation at all stages of differentiation. These findings can be explained by either a reduction in the production of lipid droplets, an increase in β-oxidation of lipids, or a combination of both. We assayed the expression of β-oxidation genes, as well as the relative level of β-oxidation during our differentiation time course using a fluorescent indicator. We found increased β-oxidation in BWS cells,

particularly around day 20, which coincided with maximal PPARA gene expression compared to control cells.

β-oxidation is a primary source of endogenous reactive oxygen species (ROS) production[47,48]. Excessive ROS can lead to oxidative stress in cells; however, cells can adapt to the stress by metabolic reprogramming and survive[63]. Even moderate changes in ROS can favor the induction of cell proliferation[64], which is essential for tumor formation. Additionally, ROS can also induce DNA damage leading to mutagenesis in nucleobases like guanine and can ultimately lead to tumor-initiating events[65]. We observed evidence of increased lipid peroxidation, a ROS by-product, in both BWS patient hepatocytes as well as in our BWS iPSC-hepatocyte model. We also report increased oxidative DNA damage in our BWS hepatocytes, in conjunction with the upregulation of the *OGG1* gene. This gene encodes 8-oxoG DNA glycosylase 1, whose product is responsible for the excision of 8-oxoguanine, a mutagenic base byproduct which occurs as a result of exposure to ROS[66]. The combination of increased oxidative DNA damage, increased lipid peroxidation, and upregulation of ROS scavenger genes in BWS hepatocytes all agrees with increased ROS production in these cells[64,67]. The role of ROS as a pathological player has been reported in various other cancers including astrocytic and ependymal glial tumors[68], colorectal cancer[69], kidney tumor[70] and breast cancers[71]. In the liver, ROS and lipid peroxidation products are known to promote the differentiation and activation of hepatic stellate cells which is important in the transition to cancer in hepatocellular carcinoma[72,73]. However, the effects on ROS on the formation of hepatoblastomas are unknown. We propose that these BWS PPARA-driven metabolomic changes, result in an increased oxidative stress environment, which can damage DNA and contribute to the transition from a cancer predisposition state to hepatoblastoma formation. In support of our findings, upregulation of PPARA signaling has been previously reported to produce oxidative DNA damage and subsequent liver carcinogenesis in several different model systems[74]. Further functional studies will be required to understand the mechanism of PPARA upregulation in BWS hepatocytes, as well as the insufficiency of increased antioxidant expression to overcome damage.

While our patient sample size was small, due to sample availability, we were able to obtain consistent data across each cohort. snRNA-seq has the ability to capture both parenchymal and nonparenchymal cells with high resolution and hence opens an avenue to study these cells in diseased and non-diseased state[10,13,14]. This approach has allowed us to examine our banked samples with single nuclei resolution. Additionally, even with the sample size limitation, we were able to replicate and extend our results in an in vitro model of BWS liver, demonstrating the validity of our findings. In subsequent studies, we will broaden our findings using a single-cell approach on freshly isolated tissue to capture more RNA signatures and underrepresented cell types in pediatric liver. Despite these limitations, our data are the first description of the transcriptomic profile in conjunction with the chromatin accessibility profile of BWS and nonBWS pediatric livers. We identified unique functional pathways enriched in the BWS liver that define its distinct metabolic function and can contribute to increased cancer incidence seen in BWS patients.

Conclusion

The current study generated, to the best of our knowledge, the largest human snRNA-seq+snATAC-seq dataset currently available comparing BWS and nonBWS pediatric liver. Taken together, our transcriptional map of pediatric liver provides a framework for understanding the metabolic nature of the BWS liver when compared to nonBWS liver. Our multiomic approach detected unique cell states within the liver and defined cellular heterogeneity in BWS and nonBWS-livers. This study also showed that the PPARA-driven metabolic state of BWS livers could be a major contributor towards BWS liver cancer predisposition. Our findings also nominate additional prophylactic therapies, such as PPARA modulators[75], for consideration in the prevention of BWS hepatoblastoma.

Methods

Patients and samples

All the samples and clinical information from patients with BWS were collected through the BWS Registry. This registry is established at the Children's Hospital of Philadelphia under the institutional review board protocol # IRB 13-010658. The liver samples of patients without BWS were collected under the Children's Hospital of Philadelphia protocol # IRB 21-018450_AM13. Informed consent was obtained for the collection of clinical information and the samples comprising this study. The limited clinical information about the nonBWS samples was extracted from the electronic clinical record through an honest broker. These samples were selected from individuals who did not have BWS (Supplementary Table 1). BWS1, BWS2, BWS3, and BWS4 represent the BWS liver cohort, while nonBWS1, nonBWS2, nonBWS3 represent the nonBWS liver cohort. The methylation profile for both the BWS and nonBWS livers were confirmed by pyrosequencing (Supplementary Fig. 2). Clinical genetic testing for BWS molecular characterization was performed in blood at the University of Pennsylvania Genetic Diagnostic Laboratory, as previously described[76]. All tumor-adjacent liver samples were collected from CHOP patients during their surgical hepatoblastoma resection and were confirmed as normal adjacent tissue beyond the tumor margins by a clinical pathologist. All the samples were snap-frozen in liquid nitrogen and stored at -80℃. All ethical regulations relevant to human research participants were followed.

Histology of livers

Control (nonBWS) tumor-adjacent and BWS tumor-adjacent liver samples were FFPE processed, sectioned, and stained using standard hematoxylin and eosin staining protocols. Sections were imaged using Leica Aperio AT2 slide scanner. Hepatocyte size was manually enumerated in FIJI by investigators blinded to cohort information. At least 2 images were analyzed per patient sample.

Single nuclei isolation

For Multiome sequencing (snRNA-seq+snATAC-seq), nuclei were isolated with Nuclei Lysis buffer [10 mM Tris-HCl, 10 mM NaCl, 3 mM $CaCl_2$, 0.1% NP-40, 0.1% Tween-20, 1% BSA, 1 mM DTT, all in 1x PBS supplemented with RNase inhibitor (1U/μL, Sigma)]. ~40–45 mg tissue was homogenized using a Dounce homogenizer in 1 ml of ice-cold Nuclei Lysis buffer and incubated on ice for 10 min with an additional 2 mL of lysis buffer. The homogenate was filtered through a 30 μm cell strainer followed by a 100 μm cell strainer. Nuclei were centrifuged at $500 \times g$ for 5 min at 4 ℃. The pellet was resuspended, washed with 1 ml of wash buffer (1x PBS + 1% BSA, 1 mM DTT supplemented with RNase inhibitor). The resultant nuclei suspension was FACS sorted using 7-Aminoactinomycin D (7-AAD) dye as a singlet discriminator on a FACS Jazz cell sorter (BD Biosciences). 600,000 sorted events were collected in 10% BSA in 1X PBS solution supplemented with RNase inhibitor. After sorting, the nuclei pellet was centrifuged at $500 \times g$ for 5 min at 4 ℃ using wash buffer and subjected to permeabilization in 100 μL 0.1X permeabilization buffer (10 mM Tris-HCl, 10 mM NaCl, 3 mM $CaCl_2$, 0.1% NP-40, 0.1% Tween-20, 1% BSA, 1 mM DTT, and 0.001% Digitonin, all in 1x PBS) for 2 min on ice. The suspended nuclei were centrifuged at $500xg$ for 5 min at 4 ℃ using the wash buffer and resuspended in 40 μL diluted nuclei buffer from 10X Genomics.

Library preparation and sequencing

10X Chromium libraries were prepared according to the manufacturer's protocol by CHOP's Center for Applied Genomics (CAG) core. All the samples were sequenced in a single sequencing run to avoid batch effect. Briefly, next-generation sequencing libraries were prepared using the 10x Genomics Chromium Single Cell Multiome Assay for Transposase-Accessible Chromatin (ATAC) and Gene Expression Reagent kit v1. ATAC libraries were uniquely indexed using the Chromium single Index Kit, pooled, and sequenced on an Illumina NovaSeq 6000 sequencer in a paired-end, dual indexing run. Gene expression libraries were uniquely indexed using the Chromium Dual Index Kit, pooled, and sequenced on an

Illumina NovaSeq 6000 sequencer in a paired-end, dual indexing run. Sequencing for each library targeted 20,000 mean reads per cell. Data was then processed using the Cell Ranger pipeline (10x Genomics, version 3.1.0) for demultiplexing and alignment of sequencing reads to the (reference hg38) transcriptome and creation of feature-barcoded count matrices for gene expression and ATAC data.

Single-nuclei RNA/ATAC 10X Multiome Sequencing

Single-nuclei RNA and single-nuclei ATAC-seq data preprocessing and quality control. The subsequent data processing involved Seurat package (version 4.9)[18–21] in R (version 4.3). Cells with transcript counts outside the 200-50000 range, >5% mitochondrial reads in snRNA-seq data, and transcriptome start site (TSS) enrichment < 4, RiboRatio > 5%, and ATAC fragments < 1000 in snATAC-seq data were excluded. Doublets were identified and removed using the DoubletFinder_v3 function from the DoubletFinder R package (version 2.0.3)[77].

Single-nuclei RNAseq data integration. After performing initial quality control (QC) as described above and removing doublets, the single nuclei RNA sequencing (snRNAseq) data was consolidated into a unified count matrix using basic R Matrix.utils. We took full advantage of Seurat's built-in functionalities for data integration. Initially, we employed "NormalizeData" to normalize the dataset. Subsequently, we applied data scaling ("ScaleData" function), accounting for mitochondrial reads ("perc.mito") and total molecule counts ("nCount_RNA") through regression. Next, we utilized "FindVariableFeatures" to select the top 2000 features using "vst" method. "RunPCA" function was used to conduct Principal Component Analysis (PCA). We retained the top 30 principal components for dimensional reduction. The resulting output served as input for Harmony[22] to mitigate batch effects with all default parameters and maximum 30 iterations using the "RunHarmony" function.

Single-nuclei RNAseq clustering and marker genes. The harmonized data underwent cell clustering via Seurat's original Louvain clustering algorithm. We first ran functions "RunUMAP". The outcome was followed by "FindNeighbors". Finally, we employed "FindClusters" at a resolution level of 0.5 to give us the read out of clustering. We tried various numbers of top PCA dimensions to better our understanding of clustering outcome. We found using the top 30 dimensions of PCA giving us most consistent results to underlying biology.

For each cluster, we identified the top 50 marker genes and their corresponding expression levels. We used the AddModuleScore feature from Seurat package with minimal expression of 20% of cells to study the distribution of the expression of the genes associated with a given liver function or state. A nonparametric statistics test "Wilcoxon Rank Sum test" was used to rank gene expression significance due to the unique nature of the single cell RNA-seq. Any gene deemed as "Marker gene" would have minimal expression fold change at 0.1 (log-scale).

Single-nuclei RNAseq cell type identification. Cell type identification was carried out primarily using marker genes which are genes ranked by magnitude of expression level change, both over-expression and under-expression, within a given cell cluster. We compared those cluster marker genes to known Cell Type Gene Markers (CTGM) through a literature search. Clusters with gene markers most consistent with CTGM were primarily labeled to the cell type CTGM associated with. Then we utilized two R packages to assist in defining the cell types within the obtained clusters. Firstly, SingleR (version 1.0.1)[78] employed the Human Primary Cell Atlas (via the R library celldex, version 1.10.1) to reference transcriptome databases, facilitating unbiased auto cell type recognition. Secondly, ScType (available at https://github.com/IanevskiAleksandr/sc-type)[79] provided another R package offering ultrafast automated methods for defining cell types in single-cell data. Finally, we examined cluster cell types identified by cluster marker genes, comparing them to cluster cell types identified by both SingleR and ScType, to assign final cell type labels to each identified cluster. Any inconsistencies that warranted further investigation were corrected by expanding the cluster marker gene list and conducting further literature research until the final cell type labels were determined.

Single nuclei RNAseq gene and functional enrichment comparing BWS patients and NonBWS controls. Gene expression levels were directly compared between the BWS tumor-adjacent liver patient group (BWS) as cases and nonBWS tumor-adjacent liver (nonBWS) as controls within each cluster. A Wilcoxon signed-rank test was used as the statistical method to rank gene expression significance. The Single Cell Pathway Analysis (SCPA) R package[80] was used to characterize the gene functional enrichment analysis within a given cluster. Gene functional annotation was collected from the Molecular Signatures Database (MSigDB) by the Broad Institute, which includes curated gene sets. Our analysis primarily focused on three curated gene set collections: "Hall-Mark", "Canonical Pathway", and "Gene Ontology". SCPA uses a multivariate distribution testing approach to identify pathways enriched in a given cell type. SCPA also provides transcriptional changes for a given pathway within each cluster. We employed the Benjamini-Hochberg (BH) correction procedure to reduce multiple testing errors.

Single-nuclei ATACseq data analysis. Analysis of single nuclei ATACseq data was performed using the ArchR package (version 1.0.2) (version 1.0.2)[23]. Cell type labels obtained from snRNAseq were transferred to ATACseq based on cell barcodes. Initially, cells within each cell type were aggregated to generate bulk ATACseq-type data using the "addGroupCoverages" function in ArchR. Chromatin accessibility peaks were identified using the "addReproduciblePeakSet" function, utilizing the MACS2 peak identification pipeline with the human genome build hg38 as a reference. Peak properties were then added with the "addPeakMatrix" function, followed by peak calling using the "getMarkerFeatures" function, which incorporated "TSSEnrichment" and "number of fragments" as covariates, and employed the Wilcoxon test as the statistical method. Marker peaks were filtered based on an absolute log fold change (log2FC) greater than 1 and a false discovery rate (FDR) less than 0.01.

Co-accessibility analysis was conducted using the "getCoAccessibility" function, with a correlation cutoff set at 0.3 and a resolution of 1. Predicted target genes for each scATAC peak were generated using the "addPeak2-GeneLinks" function with Harmony output. Subsequently, the "getPeak2-GeneLinks" function was applied, using a correlation cutoff of 0.3 and a resolution of 1. Enriched motifs were identified using the "addMotifAnnotations" function, utilizing the "cisbp" motif collection and gene annotations from EnsDb.Hsapiens.v86. This was followed by the "peakAnnoEnrichment" function, with a cutoff threshold set at FDR < 0.1 and Log2FC > 0.5. Finally, Footprint analysis was conducted using the "getFootprints" function.

Integrated snRNA-seq and snATAC-seq analysis using SCENIC plus. We integrated the snRNA-seq and snATAC seq data using single-cell multiomic inference of enhancers and gene regulatory networks (SCENIC +). SCENIC+ infers transcription factor activity and identifies potential corresponding candidate enhancer regions and regulated genes network (eRegulons)[24], and we applied it on our sn multiomic data. We first subsetted the major hepatocyte clusters (Cluster 0, 1, 7) having >500 nuclei to identify the differential eRegulon between BWS tumor-adjacent hepatocytes and the nonBWS tumor-adjacent hepatocytes. snATAC-seq data was first processed using pycisTopic[24] to identify differentially accessible regions (DARs) and sets of co-accessible regions (termed topics). A model of 40 topics were selected for motif enrichment analysis using pycisTarget[24]. Motif enrichment analysis is performed using a precomputed motif database and the motif-to-transcription factor annotation database from pycisTarget. eRegulons

were inferred by SCENIC+ using previously processed snRNA-seq data, calculated DARs and topics, and the enriched motifs. DARs were calculated using a Wilcoxon rank-sum test on the imputed probability matrix and selecting regions with a logFC > 0.5 and Benjamini–Hochberg adjusted P values < 0.05. eRegulons with negatively correlated enhancer accessibility and gene expression were filtered out. The final network was constructed using Cytoscape[81].

Induced pluripotent stem cell (iPSC) generation. A parental control iPSC line (Penn123i-SV20) was derived from adult male peripheral blood as described[82,83]. This iPSC line (referred to as SV20 or control) was cultured on Cultrex-coated plates (Biotechne) in StemMACS iPS-Brew XF medium (Miltenyi Biotech, Inc.). Medium was refreshed every other day and cells were dissociated every 4–7 days using StemMACS Passaging Solution XF (Miltenyi Biotech Inc.) and cell clumps were passaged at a ratio of 1:8-1:30. A CRISPR/Cas 9 approach was used to delete a ~ 1.7 kb portion of the second imprinting center of the maternal chromosome in SV20 in order to create imprinted center 2 loss of methylation (IC2 LOM) lines (chr11:2699181-2700857, Supplementary Fig. 7a). This region was chosen, as it overlaps with several reported BWS patient deletions[37–41]. In order to achieve this, two guide RNAs with low off-target potential were designed (https://cripor.gi.ucsc.edu) and synthesized (Synthego). 50 pmol of Guide 1 (5′-CGGGTCTATAGTTCTCATGG(TGG)-3′) and 50 pmol of Guide 2 (5′-GGCAATGCTTGGCATTCAGA(AGG)-3′) together with 16.5 pmol of Alt-R S.p.HiFi Cas9 Nuclease V3 were transfected by nucleofection into SV20 cells using the Amaxa 4D-Nucleofactor. After 2 days of culture, cells were lifted with Accutase (Diagnocine) and single cells were seeded at a low density (1000 cells per 10 cm in a Cultrex-coated dish) in StemMACS iPS-Brew XF medium containing CloneR2 (STEMCELL Technology). Colonies derived from single cells were manually picked after around 8 days of seeding, and genomic DNAs were isolated using QuickExtract DNA Extraction solution (VWR). Deletion of the ~1.7 kb portion and the zygosity of the resulting clones were determined by PCR, followed by Sanger sequencing, using 3 pairs of primers (Supplementary Fig. 7g; primers 1 + 4; primers 1 + 2; and primers 3 + 4). Two lines (3H5, 3D1, referred to as BWS 1 and BWS 2, respectively) were generated with this strategy and were confirmed by genotyping. G-banded karyotyping was performed by Cell Line Genetics (https://clgenetics.com) to confirm a normal genotype. The methylation patterns at IC1 and IC2 were confirmed by pyrosequencing (Supplementary Fig. 7d, 7e). For the 3H5 (BWS1) line, the maternal allele has an expected deletion at chr11:2699181-2700857 and the paternal allele has small deletions at chr11:2699166-2699175, 2700856, 2700858-2700859, and one mutation at chr11:2700863 (T to A) due to Cas9 cutting at one guide RNA site and subsequent non-homologous end joining repairs associated with CRISPR/Cas9 editing. Similarly, for the 3D1 (BWS2) line, the maternal allele has an expected deletion at chr11:2699181-2700859 with an additional 2 base pair deletion, while the paternal allele has a small deletion at chr11:2699159-2699168 and an insertion at chr11:2700864-2700865 (GA to GGA).

iPSC differentiation. Parental control line and two BWS IC2 LOM lines (BWS 1, BWS 2) were plated on laminin-coated plates. 0.5×10^6 cells were seeded per well in a 24-well plate. Cells were subjected to a 20-day protocol for hepatocyte differentiation using the STEMdiff hepatocyte kit (Stem Cell Technologies), according to the manufacturer's instructions. This 2-dimensional differentiation system contains different culture medias to generate endoderm lineage cells, then hepatic progenitor cells, and finally hepatocytes, at defined times post plating. Cells were imaged by brightfield/phase microscopy throughout the protocol using an EVOS M7000 imaging system to monitor differentiation.

RNA isolation, cDNA synthesis, and quantitative RT-PCR (qRT-PCR). 5×10^5 Control and BWS IC2 LOM iPSCs were seeded into 12 well laminin-coated plates. Cells were differentiated for 5, 10, 15, 18, and

20 days with the STEMDiff hepatocyte kit (Stem Cell Technologies), according to the manufacturer's instructions. RNA was isolated with Trizol (Thermo Fisher Scientific) and reverse transcribed to cDNA with an iScript cDNA synthesis kit (Bio-Rad). Quantitative real time PCR was conducted in technical triplicates or quadruplicates and 4 biological replicates for each data point. Gene expression was quantified using a multiplexed ddCT method, using *B2M* as a housekeeping gene. All primers with TaqMan probes were purchased from Thermo Fisher Scientific. Gene assay ID's: FAM-*CXCR4* (Hs00976734_m1), FAM-*FOXA2* (Hs00232764_m1), FAM-*SOX17* (Hs00751752_s1), FAM-*PPARA* (Hs00947536_m1), and VIC-*B2M* (Hs00187842_m1).

iPSC to hepatocyte live cell staining, imaging, and analysis. iPSCs were differentiated and used for assays at timepoints of Day 10, Day 15, Day 18, and Day 20 of the hepatocyte differentiation protocol. Cells were stained for at 37 °C in the dark with either 2.5 µM Bodipy 493 (to assess neutral lipids; Invitrogen #D3922; one-hour incubation), 2 µM FAOBlue (to assess fatty acid β-oxidation; Diagnocine #FNK-FDV-0033; two-hour incubation) or 10 µM Acrolein red (lipid peroxidation and oxidative stress; Diagnocine #FNK-FDV-0022; one-hour incubation) in HEPES-buffered saline (HBS). Cells were washed with HBS and imaged live with an EVOS M7000 imaging system equipped with a GFP filter, a BFP-tag filter, and a Texas red filter, respectively. Data was collected by imaging of 4 random fields from at least 2 biological replicates per time point. Analysis of intensities were conducted in FIJI and normalized to cell number by independent investigators.

Bulk RNAseq and analysis. Undifferentiated iPSCs (Sv20, 3D1, 3H5) and iPSCs (Sv20, 3D1, 3H5) undergoing hepatocyte differentiation at D15 and D20 were collected in two biological replicates from 24-well plates. Briefly, cells were washed with cold PBS, scraped off of the plates with cell scrapers, resuspended in 1 mL cold PBS, and centrifuged at $300 \times g$ for 5 min at 4 °C. Cell pellets were snap frozen in liquid nitrogen and stored at –80 °C. RNA extraction and bulk RNA sequencing was conducted by the CHOP Center for Applied Genomics (CAG) core. In brief, RNA extraction was performed using AllPrep DNA/RNA Micro Kit (QIAGEN). RNA eluate concentration was quantified using the QUBIT HS RNA kit (Thermo Fisher) and quality was assessed by TapeStation (Agilent). All sample libraries were prepared using Illumina Stranded Total RNAseq library prep kit with 300 ng of total RNA input to start. The libraries were then sequenced on a NovaSeq 6000 instrument with a v1.5 S1 200 cycles kit (101 × 101, Illumina).

The FASTQ files were subjected to quality check as described[84,85]. The reads were aligned with Hisat2[86] to the hg38 reference genome. The feature counts were then extracted using featureCounts[87], followed by differential gene expression analysis using the Deseq2 R package[88]. Differentially expressed genes were analyzed using a hypergeometric test and the Benjamini & Hochberg method. Genes of interest were displayed as either log2 fold change relative to control, transformed read counts, or filtered based on specific gene lists and displayed as volcano plots. The transformed read counts were generated using variance stabilizing transformation (VST) calculated by the DESeq2 method. The transformed read counts were used for visualizing the expression trend of hepatocyte genes. The volcano plots were used to agnostically display the significant differentially expressed genes enriched in the selected pathway. The genes for the selected pathway were obtained from the Molecular Signature Database for Gene Set Enrichment Analysis (GSEA) by Broad Institute. The volcano plot displays genes with p value < 0.05 and log2 fold change >0.75.

DNA extraction and bisulfite conversion (pre-pyrosequencing). Genomic DNA from liver samples and iPSC-derived cells were isolated using the AllPrep DNA/RNA Micro Kit (Qiagen) and quantified on Qubit with HS DNA kit (Thermo Fisher). 100–500 ng of DNA was bisulfite converted using the EpiTect bisulfite kit (Qiagen), according to the manufacturer's instructions.

Pyrosequencing. Pyrosequencing was performed on bisulfite-converted DNA using the Pyromark PCR kit (Qiagen), and sequencing was performed on a Pyromark Q48 Autoprep (Qiagen). Sequencing primers are listed in Supplementary Table 4. Note: One BWS liver contained a single nucleotide polymorphism in H19 primer set 1, so BWS livers were assessed for methylation using H19 primer set 2.

iPSC-derived hepatocyte cell size. Cells were grown on coverglass and were fixed in 4% paraformaldehyde in PBS for 10 min and washed twice with PBS. Fixed cells were permeabilized with saponin (0.5% in PBS) for 10 min, washed with PBS, and stained with Alexa Fluor 647 Phalloidin (1/50; Cell Signaling #8940S) in PBS in the dark for 30 min. Cells were washed three times with PBS and mounted on slides with Prolong gold with DAPI (Fisher Scientific). Cells were imaged on a Nikon Ti-2 inverted microscope. At least 3 biological replicates were analyzed per sample.

8-oxyoguanine staining of differentiated iPSCs. Day 20-differentiated hepatocytes were fixed in 4% PFA/PBS for 10 min, washed twice with PBS, 3 min each, and permeabilized with 0.5% triton X-100/PBS for 10 min. Cells were washed and incubated with DNase-free RNAse A (100 µg/mL; Fermentas/Fisher Scientific) for 20 min at 37 °C to remove any oxidative RNA damage. Cells were washed with PBS twice, for 3 min each and then incubated with 2 N HCl for 30 min at 37 °C. Acid solution was aspirated and neutralized by washing with 0.1 M Borate buffer, pH 8.5 (Thermo Fisher Scientific) three times for 3 min each. Cells were subsequently washed with PBS twice for 3 min each and blocked at room temperature with 3% BSA/PBS containing 0.1% triton X-100 for one hour. Primary antibody to 8-oxyoguanine (Rockland #200-301-A99; 1/200) was diluted in blocking buffer overnight at 4 °C. Cells were washed twice with PBS and incubated with Donkey anti-mouse Alexa Fluor 488 IgG (Fisher #A-21202, 1/2,000) for one hour at room temperature. Cells were stained with DAPI (10 µg/mL) for 5 min and washed with PBS before imaging on a Nikon Ti-2 inverted microscope. At least 3 biological replicates were analyzed per line.

Statistics and reproducibility. Patient samples for this study included 3 nonBWS and 4 BWS livers for the multiome arm of the study, while histological analysis included 4 nonBWS and 11 BWS livers. For hepatocyte size analysis, each data point is a measured cell. For iPSC experiments, data were generated from one parental control line and 2 engineered BWS lines. Data points for iPSC derived data represent either individual hepatocytes (for size measurements) or biological replicates (for all other assays). Graphpad prism v10.4.1 software was used for graphical depiction of data and analyses related to liver hepatocyte size, qRT-PCR, pyrosequencing results, and iPSC functional characterization. Displayed are mean ± SEM or mean ± SD, as indicated in the respective figure legend. Analysis was conducted using t tests with Welch's correction or by ANOVA. p values of <0.05 were considered statistically significant. For sequencing data displayed in R, statistics were conducted using the Wilcoxon rank sum test. Benjamini-Hochberg adjusted p values of less than 0.05 were considered significant.

Biological materials availability
BWS iPSC lines can be obtained upon reasonable request to the corresponding author and obtaining a material transfer agreement.

Reporting summary
Further information on research design is available in the Nature Portfolio Reporting Summary linked to this article.

Data availability
Raw sequencing data from patient samples (snRNA-seq, snATAC-seq) were deposited in dbGAP with accession number phs002614.v2.p1. Authorized access to this dbGAP dataset is possible with contact to the corresponding author, as dictated in the research study IRB protocol stipulations. Bulk RNA sequencing from iPSCs and differentiated hepatocytes were uploaded to the GEO repository with accession number GSE269947. The authors declare that all R scripts supporting the findings of this study are available from the corresponding author upon reasonable request. Data values used for graphpad prism graphs can be found in Supplementary Data File 4.

Code availability
This study did not generate any unique code. All software tools used in this study are publicly available.

References
1. Nirgude S., Naveh N. S. S., Kavari S. L., Traxler E. M., Kalish J. M. Cancer predisposition signaling in Beckwith-Wiedemann Syndrome drives Wilms tumor development. *Br J Cancer*, (2023).
2. Klein, SD, DeMarchis, M, Linn, RL, MacFarland, SP & Kalish, JM Occurrence of Hepatoblastomas in Patients with Beckwith-Wiedemann Spectrum (BWSp). *Cancers (Basel)* **15**, 2548 (2023).
3. Sobel Naveh, NS, Traxler, EM, Duffy, KA & Kalish, JM Molecular networks of hepatoblastoma predisposition and oncogenesis in Beckwith-Wiedemann syndrome. *Hepatol. Commun.* **6**, 2132–2146 (2022).
4. Duffy, KA et al. Characterization of the Beckwith-Wiedemann spectrum: Diagnosis and management. *Am. J. Med Genet C. Semin Med. Genet* **181**, 693–708 (2019).
5. Si-Tayeb, K, Lemaigre, FP & Duncan, SA Organogenesis and development of the liver. *Dev. Cell* **18**, 175–189 (2010).
6. Mitra, V & Metcalf, J Metabolic functions of the liver. *Anaesth. Intensive Care Med.* **10**, 334–335 (2009).
7. Rui, L Energy metabolism in the liver. *Compr. Physiol.* **4**, 177–197 (2014).
8. Bogdanos, DP, Gao, B & Gershwin, ME Liver immunology. *Compr. Physiol.* **3**, 567–598 (2013).
9. MacParland, SA et al. Single cell RNA sequencing of human liver reveals distinct intrahepatic macrophage populations. *Nat. Commun.* **9**, (2018). 4383.
10. Andrews, TS et al. Single-Cell, Single-Nucleus, and Spatial RNA Sequencing of the Human Liver Identifies Cholangiocyte and Mesenchymal Heterogeneity. *Hepatol. Commun.* **6**, 821–840 (2022).
11. Wesley, BT et al. Single-cell atlas of human liver development reveals pathways directing hepatic cell fates. *Nat. Cell Biol.* **24**, 1487–1498 (2022).
12. Payen, VL et al. Single-cell RNA sequencing of human liver reveals hepatic stellate cell heterogeneity. *JHEP Rep.* **3**, (2021). 100278.
13. Andrews, TS et al. Single-cell, single-nucleus, and spatial transcriptomics characterization of the immunological landscape in the healthy and PSC human liver. *J. Hepatol.* **80**, 730–743 (2024).
14. Guilliams, M et al. Spatial proteogenomics reveals distinct and evolutionarily conserved hepatic macrophage niches. *Cell* **185**, 379–396 e338 (2022).
15. Duffy, KA, Cohen, JL, Elci, OU & Kalish, JM Development of the Serum alpha-Fetoprotein Reference Range in Patients with Beckwith-Wiedemann Spectrum. *J. Pediatr.* **212**, 195–200 e192 (2019).
16. Muto, Y et al. Single cell transcriptional and chromatin accessibility profiling redefine cellular heterogeneity in the adult human kidney. *Nat. Commun.* **12**, 2190 (2021).
17. Chang, S & Bartolomei, MS Modeling human epigenetic disorders in mice: Beckwith-Wiedemann syndrome and Silver-Russell syndrome. *Dis. Model Mech.* **13**, dmm044123 (2020).
18. Hao, Y et al. Integrated analysis of multimodal single-cell data. *Cell* **184**, 3573–3587 e3529 (2021).
19. Stuart, T et al. Comprehensive Integration of Single-Cell Data. *Cell* **177**, 1888–1902 e1821 (2019).

20. Butler, A, Hoffman, P, Smibert, P, Papalexi, E & Satija, R Integrating single-cell transcriptomic data across different conditions, technologies, and species. *Nat. Biotechnol.* **36**, 411–420 (2018).

21. Satija, R, Farrell, JA, Gennert, D, Schier, AF & Regev, A Spatial reconstruction of single-cell gene expression data. *Nat. Biotechnol.* **33**, 495–502 (2015).

22. Korsunsky, I et al. Fast, sensitive and accurate integration of single-cell data with Harmony. *Nat. Methods* **16**, 1289–1296 (2019).

23. Granja, JM et al. ArchR is a scalable software package for integrative single-cell chromatin accessibility analysis. *Nat. Genet* **53**, 403–411 (2021).

24. Bravo Gonzalez-Blas, C et al. SCENIC+: single-cell multiomic inference of enhancers and gene regulatory networks. *Nat. Methods* **20**, 1355–1367 (2023).

25. Rakhshandehroo, M, Knoch, B, Müller, M & Kersten, S Peroxisome Proliferator-Activated Receptor Alpha Target Genes. *PPAR Res.* **2010**, (2010). 612089.

26. Changizi, Z, Kajbaf, F & Moslehi, A An Overview of the Role of Peroxisome Proliferator-activated Receptors in Liver Diseases. *J. Clin. Transl. Hepatol.* **11**, 1542–1552 (2023).

27. Brocker, CN et al. Hepatocyte-specific PPARA expression exclusively promotes agonist-induced cell proliferation without influence from nonparenchymal cells. *Am. J. Physiol. Gastrointest. Liver Physiol.* **312**, G283–G299 (2017).

28. Fan, S et al. YAP-TEAD mediates PPAR alpha-induced hepatomegaly and liver regeneration in mice. *Hepatology* **75**, 74–88 (2022).

29. Shan, J et al. Tcf7l1 Acts as a Suppressor for the Self-Renewal of Liver Cancer Stem Cells and Is Regulated by IGF/MEK/ERK Signaling Independent of beta-Catenin. *Stem Cells* **37**, 1389–1400 (2019).

30. Pu, XY et al. Overexpression of transcription factor 3 drives hepatocarcinoma development by enhancing cell proliferation via activating Wnt signaling pathway. *Hepatobiliary Pancreat. Dis. Int* **21**, 378–386 (2022).

31. Todisco, S et al. PPAR Alpha as a Metabolic Modulator of the Liver: Role in the Pathogenesis of Nonalcoholic Steatohepatitis (NASH). *Biol. (Basel)* **11**, 792 (2022).

32. Aibara, D et al. Gene repression through epigenetic modulation by PPARA enhances hepatocellular proliferation. *iScience* **25**, (2022). 104196.

33. Szklarczyk, D et al. The STRING database in 2021: customizable protein-protein networks, and functional characterization of user-uploaded gene/measurement sets. *Nucleic Acids Res* **49**, D605–D612 (2021).

34. Szalowska, E, Tesfay, HA, van Hijum, SA & Kersten, S Transcriptomic signatures of peroxisome proliferator-activated receptor alpha (PPARalpha) in different mouse liver models identify novel aspects of its biology. *BMC Genomics* **15**, (2014). 1106.

35. Nakamura, MT, Yudell, BE & Loor, JJ Regulation of energy metabolism by long-chain fatty acids. *Prog. Lipid Res* **53**, 124–144 (2014).

36. Houten, SM, Violante, S, Ventura, FV & Wanders, RJ The Biochemistry and Physiology of Mitochondrial Fatty Acid beta-Oxidation and Its Genetic Disorders. *Annu. Rev. Physiol.* **78**, 23–44 (2016).

37. Baskin, B et al. High frequency of copy number variations (CNVs) in the chromosome 11p15 region in patients with Beckwith-Wiedemann syndrome. *Hum. Genet* **133**, 321–330 (2014).

38. Gurrieri, F et al. Mild Beckwith-Wiedemann and severe long-QT syndrome due to deletion of the imprinting center 2 on chromosome 11p. *Eur. J. Hum. Genet* **21**, 965–969 (2013).

39. Niemitz, EL et al. Microdeletion of LIT1 in familial Beckwith-Wiedemann syndrome. *Am. J. Hum. Genet* **75**, 844–849 (2004).

40. Algar, E, Dagar, V, Sebaj, M & Pachter, N An 11p15 imprinting centre region 2 deletion in a family with Beckwith Wiedemann syndrome provides insights into imprinting control at CDKN1C. *PLoS One* **6**, e29034 (2011).

41. Zollino, M et al. A case of Beckwith-Wiedemann syndrome caused by a cryptic 11p15 deletion encompassing the centromeric imprinted domain of the BWS locus. *J. Med Genet* **47**, 429–432 (2010).

42. Holtzinger, A et al. New markers for tracking endoderm induction and hepatocyte differentiation from human pluripotent stem cells. *Development* **142**, 4253–4265 (2015).

43. Spangenburg, EE, Pratt, SJP, Wohlers, LM & Lovering, RM Use of BODIPY (493/503) to visualize intramuscular lipid droplets in skeletal muscle. *J. Biomed. Biotechnol.* **2011**, 598358 (2011).

44. Qiu, B & Simon, MC BODIPY 493/503 Staining of Neutral Lipid Droplets for Microscopy and Quantification by Flow Cytometry. *Bio Protoc.* **6**, e1912 (2016).

45. van der Weijden, VA et al. FOXO1-mediated lipid metabolism maintains mammalian embryos in dormancy. *Nat. Cell Biol.* **26**, 181–193 (2024).

46. Tian, G et al. Voltage-dependent anion channel 1 (VDAC1) overexpression alleviates cardiac fibroblast activation in cardiac fibrosis via regulating fatty acid metabolism. *Redox Biol.* **67**, 102907 (2023).

47. Rosca, MG et al. Oxidation of fatty acids is the source of increased mitochondrial reactive oxygen species production in kidney cortical tubules in early diabetes. *Diabetes* **61**, 2074–2083 (2012).

48. Chen, Z, Tian, R, She, Z, Cai, J & Li, H Role of oxidative stress in the pathogenesis of nonalcoholic fatty liver disease. *Free Radic. Biol. Med.* **152**, 116–141 (2020).

49. Miyamoto, HD et al. Iron Overload via Heme Degradation in the Endoplasmic Reticulum Triggers Ferroptosis in Myocardial Ischemia-Reperfusion Injury. *JACC Basic Transl. Sci.* **7**, 800–819 (2022).

50. Tanei, T et al. Cascade Reaction in Human Live Tissue Allows Clinically Applicable Diagnosis of Breast Cancer Morphology. *Adv. Sci. (Weinh.)* **6**, (2019). 1801479.

51. Srinivas, US, Tan, BWQ, Vellayappan, BA & Jeyasekharan, AD ROS and the DNA damage response in cancer. *Redox Biol.* **25**, 101084 (2019).

52. Sane, S & Rezvani, K Essential Roles of E3 Ubiquitin Ligases in p53 Regulation. *Int J. Mol. Sci.* **18**, 442 (2017).

53. Thakar, T & Moldovan, GL The emerging determinants of replication fork stability. *Nucleic Acids Res* **49**, 7224–7238 (2021).

54. Coquel, F et al. SAMHD1 acts at stalled replication forks to prevent interferon induction. *Nature* **557**, 57–61 (2018).

55. Alnajjar, KS & Sweasy, JB A new perspective on oxidation of DNA repair proteins and cancer. *DNA Repair (Amst.)* **76**, 60–69 (2019).

56. Gornicka, A et al. Transcriptional profile of genes involved in oxidative stress and antioxidant defense in a dietary murine model of steatohepatitis. *Antioxid. Redox Signal* **15**, 437–445 (2011).

57. Wang, Y, Nakajima, T, Gonzalez, FJ & Tanaka, N PPARs as Metabolic Regulators in the Liver: Lessons from Liver-Specific PPAR-Null Mice. *Int J. Mol. Sci.* **21**, 2061 (2020).

58. Mello, T, Polvani, S & Galli, A Peroxisome proliferator-activated receptor and retinoic x receptor in alcoholic liver disease. *PPAR Res* **2009**, (2009). 748174.

59. Jusakul, A, Yongvanit, P, Loilome, W, Namwat, N & Kuver, R Mechanisms of oxysterol-induced carcinogenesis. *Lipids Health Dis.* **10**, 44 (2011).

60. de Freitas, FA, Levy, D, Zarrouk, A, Lizard, G & Bydlowski, SP Impact of Oxysterols on Cell Death, Proliferation, and Differentiation Induction: Current Status. *Cells* **10**, 2301 (2021).

61. Bjorkhem, I Do oxysterols control cholesterol homeostasis?. *J. Clin. Invest* **110**, 725–730 (2002).

62. Talari, NK et al. Lipid-droplet associated mitochondria promote fatty-acid oxidation through a distinct bioenergetic pattern in male Wistar rats. *Nat. Commun.* **14**, 766 (2023).

63. Hayes, JD, Dinkova-Kostova, AT & Tew, KD Oxidative Stress in Cancer. *Cancer Cell* **38**, 167–197 (2020).

64. Barrera, G Oxidative stress and lipid peroxidation products in cancer progression and therapy. *ISRN Oncol.* **2012**, 137289. (2012).

65. Harris, IS & DeNicola, GM The Complex Interplay between Antioxidants and ROS in Cancer. *Trends Cell Biol.* **30**, 440–451 (2020).

66. Wang, R, Hao, W, Pan, L, Boldogh, I & Ba, X The roles of base excision repair enzyme OGG1 in gene expression. *Cell Mol. Life Sci.* **75**, 3741–3750 (2018).

67. Su, LJ et al. Reactive Oxygen Species-Induced Lipid Peroxidation in Apoptosis, Autophagy, and Ferroptosis. *Oxid. Med Cell Longev.* **2019**, 5080843 (2019).

68. Juric-Sekhar, G, Zarkovic, K, Waeg, G, Cipak, A & Zarkovic, N Distribution of 4-hydroxynonenal-protein conjugates as a marker of lipid peroxidation and parameter of malignancy in astrocytic and ependymal tumors of the brain. *Tumori* **95**, 762–768 (2009).

69. Skrzydlewska, E, Stankiewicz, A, Sulkowska, M, Sulkowski, S & Kasacka, I Antioxidant status and lipid peroxidation in colorectal cancer. *J. Toxicol. Environ. Health A* **64**, 213–222 (2001).

70. Oberley, TD, Toyokuni, S & Szweda, LI Localization of hydroxynonenal protein adducts in normal human kidney and selected human kidney cancers. *Free Radic. Biol. Med.* **27**, 695–703 (1999).

71. Karihtala, P, Kauppila, S, Puistola, U & Jukkola-Vuorinen, A Divergent behaviour of oxidative stress markers 8-hydroxydeoxyguanosine (8-OHdG) and 4-hydroxy-2-nonenal (HNE) in breast carcinogenesis. *Histopathology* **58**, 854–862 (2011).

72. Allameh A., Niayesh-Mehr R., Aliarab A., Sebastiani G., Pantopoulos K. Oxidative Stress in Liver Pathophysiology and Disease. *Antioxidants (Basel)* **12**, (2023).

73. Gandhi, CR Oxidative Stress and Hepatic Stellate Cells: A PARADOXICAL RELATIONSHIP. *Trends Cell Mol. Biol.* **7**, 1–10 (2012).

74. Klaunig, JE, Kamendulis, LM & Hocevar, BA Oxidative stress and oxidative damage in carcinogenesis. *Toxicol. Pathol.* **38**, 96–109 (2010).

75. Tan, Y et al. PPAR-alpha Modulators as Current and Potential Cancer Treatments. *Front Oncol.* **11**, (2021). 599995.

76. Baker, SW et al. Improved molecular detection of mosaicism in Beckwith-Wiedemann Syndrome. *J. Med Genet* **58**, 178–184 (2021).

77. McGinnis, CS, Murrow, LM & Gartner, ZJ DoubletFinder: Doublet Detection in Single-Cell RNA Sequencing Data Using Artificial Nearest Neighbors. *Cell Syst.* **8**, 329–337 e324 (2019).

78. Aran, D et al. Reference-based analysis of lung single-cell sequencing reveals a transitional profibrotic macrophage. *Nat. Immunol.* **20**, 163–172 (2019).

79. Ianevski, A, Giri, AK & Aittokallio, T Fully-automated and ultra-fast cell-type identification using specific marker combinations from single-cell transcriptomic data. *Nat. Commun.* **13**, 1246 (2022).

80. Bibby, JA et al. Systematic single-cell pathway analysis to characterize early T cell activation. *Cell Rep.* **41**, (2022). 111697.

81. Shannon, P et al. Cytoscape: a software environment for integrated models of biomolecular interaction networks. *Genome Res* **13**, 2498–2504 (2003).

82. Yang, W et al. Generation of iPSCs as a Pooled Culture Using Magnetic Activated Cell Sorting of Newly Reprogrammed Cells. *PLoS One* **10**, e0134995 (2015).

83. Pashos, EE et al. Large, Diverse Population Cohorts of hiPSCs and Derived Hepatocyte-like Cells Reveal Functional Genetic Variation at Blood Lipid-Associated Loci. *Cell Stem Cell* **20**, 558–570 e510 (2017).

84. Nirgude, S, Desai, S & Choudhary, B Curcumin alters distinct molecular pathways in breast cancer subtypes revealed by integrated miRNA/mRNA expression analysis. *Cancer Rep. (Hoboken)* **5**, e1596. (2022).

85. Nirgude, S, Desai, S, Mahadeva, R, Ravindran, F & Choudhary, B ST08 Altered NF-kappaB Pathway in Breast Cancer Cells In Vitro as Revealed by miRNA-mRNA Analysis and Enhanced the Effect of Cisplatin on Tumour Reduction in EAC Mouse Model. *Front Oncol.* **12**, 835027 (2022).

86. Kim, D, Paggi, JM, Park, C, Bennett, C & Salzberg, SL Graph-based genome alignment and genotyping with HISAT2 and HISAT-genotype. *Nat. Biotechnol.* **37**, 907–915 (2019).

87. Liao, Y, Smyth, GK & Shi, W featureCounts: an efficient general purpose program for assigning sequence reads to genomic features. *Bioinformatics* **30**, 923–930 (2014).

88. Love, MI, Huber, W & Anders, S Moderated estimation of fold change and dispersion for RNA-seq data with DESeq2. *Genome Biol.* **15**, 550 (2014).

Author contributions

S.N., E.D.T., and J.M.K. designed the study. S.N., E.D.T., S.L.K., and R.D.P. performed experiments. S.N., E.D.T., Z.L., S.L.K., R.D.P., M.B., S.M, and M.X. analyzed the data. B.M., L.G.G, and K.M.B provided materials as part of the CHOP biobank and/or clinical data. F.W. and W.Y. generated iPSC lines as part of the Upenn iPSC core facility. S.N., E.D.T., and J.M.K. wrote the manuscript.

Competing interests

The authors declare no competing interests.

Additional information

Supplementary information The online version contains supplementary material available at https://doi.org/10.1038/s42003-025-07961-9.

Correspondence and requests for materials should be addressed to Jennifer M. Kalish.

Peer review information *Communications Biology* thanks the anonymous reviewers for their contribution to the peer review of this work. Primary Handling Editors: Simona Chera & Rosie Bunton-Stasyshyn.

Reprints and permissions information is available at http://www.nature.com/reprints

Publisher's note Springer Nature remains neutral with regard to jurisdictional claims in published maps and institutional affiliations.